

7-6-2016

Wavefront Sensor

Richard Mulé
Santa Clara University

Follow this and additional works at: http://scholarcommons.scu.edu/elec_senior

 Part of the [Electrical and Computer Engineering Commons](#)

Recommended Citation

Mulé, Richard, "Wavefront Sensor" (2016). *Electrical Engineering Senior Theses*. Paper 30.

This Thesis is brought to you for free and open access by the Student Scholarship at Scholar Commons. It has been accepted for inclusion in Electrical Engineering Senior Theses by an authorized administrator of Scholar Commons. For more information, please contact rscroggin@scu.edu.

SANTA CLARA UNIVERSITY

Department of Electrical Engineering

I HEREBY RECOMMEND THAT THE THESIS PREPARED
UNDER MY SUPERVISION BY

Richard Mulé

ENTITLED

Wavefront Sensor

BE ACCEPTED IN PARTIAL FULFILLMENT OF THE REQUIREMENTS
FOR THE DEGREE OF

**BACHELOR OF SCIENCE
IN
ELECTRICAL ENGINEERING**



Thesis Advisor

30 June 2016

date



Thesis Advisor

20 June 2016

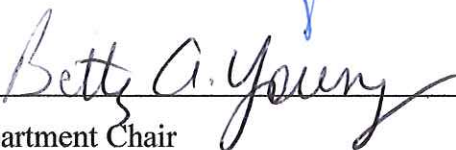
date



Department Chair

20 June 2016

date



Department Chair

July 6, 2016

date

Wavefront Sensor

By

Richard Mulé

SENIOR DESIGN PROJECT REPORT

Submitted to
the Department of Electrical Engineering

of

SANTA CLARA UNIVERSITY

in Partial Fulfillment of the Requirements
for the degree of
Bachelor of Science in Electrical Engineering

Santa Clara, California

2016

ABSTRACT

Wavefront reconstruction techniques have enabled important scientific improvements to corrective imaging in astronomy, optometry, and elsewhere. Here, we describe the design of a wavefront reconstruction-based adaptive optics system designed at Santa Clara University (SCU) in the Department of Physics. Our compact system is based on a modified Shack-Hartmann sensor design and can detect wavefront disturbances on the order of tens of nanometers. The full SCU system includes a 635 nm laser, a collimating lens pair, two mirrors, a microlens array, and a commercial CCD camera. The CCD data is analyzed using a least-squares reconstruction algorithm. Here, we present preliminary wavefront reconstruction results obtained with our setup for wavefront perturbations caused by either lens tilt effects or heat-induced air density fluctuations.

Keywords: Wavefront sensor, adaptive optics, wavefront reconstruction

Acknowledgments

I would like to thank the Santa Clara University Physics Department for its support and for funding the project. Additionally, I wish to thank my advisors Dr. Chris Weber from the Physics Department and Dr. Sally Wood from the Electrical Engineering Department for their expertise and guidance. Moreover, I am grateful to Dr. Weber for providing this opportunity to continue my study of optics and give back to Santa Clara's academic community. Lastly, I would like to thank Dr. Betty Young, the Physics Department Chair, for all of her help during the editing process.

Table of Contents

Chapter 1: Introduction	2
1.1 Project Objectives.....	2
1.2 Background and Related Work.....	2
Chapter 2: Experimental Setup	4
2.1 Implementation.....	4
2.1.1 Microlens Array.....	4
2.1.2 CCD Array.....	5
Chapter 3: Wavefront Phase Shift Reconstruction Algorithm	6
3.1 Image Acquisition and Noise Elimination.....	6
3.2 Weighted Centroid Determination of CCD Pixel Bright-Spots.....	7
3.3 Gradient Computation.....	8
3.4 Hudgin Geometry.....	8
Chapter 4: Results	10
4.1 Flat Wavefront.....	10
4.2 Experimental Noise.....	10
4.3 Wavefront Perturbed by a Soldering Iron.....	11
4.4 Wavefront Perturbed by a Mechanical Shear to the System.....	12
Chapter 5: Bill of Materials	14
Chapter 6: Professional Issues and Constraints	15
6.1 Ethical Analysis.....	15
6.1.1 Organizational Considerations.....	15
6.1.2 Social Considerations.....	15
6.1.3 Research & Design Considerations.....	16
6.1.4 Summary.....	16
6.2 Health and Safety.....	17
6.3 STS and Civic Engagement.....	17
6.4 Manufacturability and Usability.....	17
6.5 Sustainability and Environmental Impact.....	18
Chapter 7: Conclusion	19
Works Cited	20

APPENDICES

Appendix A: HeNe Laser Datasheet.....	23
Appendix B: NI PCI 1405 Datasheet.....	25
Appendix C: MLA150-7AR Datasheet.....	27
Appendix D: Matlab Code.....	30

LIST OF FIGURES

1. Visual Representation of Shack-Hartmann Sensor.....	2
2. Functional Block Diagram.....	3
3. Magnified Image of Microlens array.....	4
4. Transmission Spectrum of Microlens Array.....	4
5. Raw Image of CCD Data.....	6
6. Magnified View of Noise in CCD Data.....	6
7. Magnified Plot of a Flat Wavefront and a Wavefront Perturbed by Soldering Iron.....	7
8. Numbering Convention of 4x4 Hudgin Geometry.....	9
9. 4x4 Matrix of Hudgin Gradient Relationships.....	9
10. Phase Plot of Identical Wavefronts.....	12
11. Centroid Plot of a Wavefront Peturbed by Noise.....	12
12. Phase Plot of a Wavefront Peturbed by Noise.....	13
13. Centroid Plot of a Wavefront Perturbed by Soldering Iron.....	13
14. Phase Plot of a Wavefront Perturbed by Soldering Iron.....	14
15. Centroid Plot of a Wavefront Sheared in the x-direction.....	14
16. Centroid Plot of a Wavefront Sheared in the y-direction.....	14
17. Phase Plot of a Wavefront Sheared in the x-direction.....	15
18. Phase Plot of a Wavefront Sheared in the y-direction.....	15

Chapter 1: Introduction

1.1 Project Objectives

The Santa Clara University Physics Department hopes to incorporate wavefront sensing technology into the optics curriculum to improve students' understanding of advanced electromagnetic and optical phenomena, enhance the undergraduate laboratory experience, and facilitate future research in optics. My project aimed to satisfy that need by developing a wavefront sensor that could visually reconstruct perturbed wavefronts, be used by students with minimal coding experience, be readily adapted to new experiments, enable researchers to map disturbances on the order microns, and operate with a low noise level on the order of tens of nanometers. Further, I hoped to construct the system using components and equipment already owned by SCU Physics, saving them (and potentially scientists and engineers at other universities who demonstrate interest) several thousands of dollars otherwise required to purchase a commercial wavefront sensor system..

1.2 Background and Related Work

Wavefront sensing techniques were first developed in the early 1900s by Johannes Hartmann who hoped to advance the field of optical metrology (Migdal et al. 229). A modernized implementation of his technique is shown schematically in Figure 1. In the Hartmann method, collimated light shines on an opaque aperture with holes. The holes discretize the incident light into small spots that appear in the focal plane of the aperture. Any

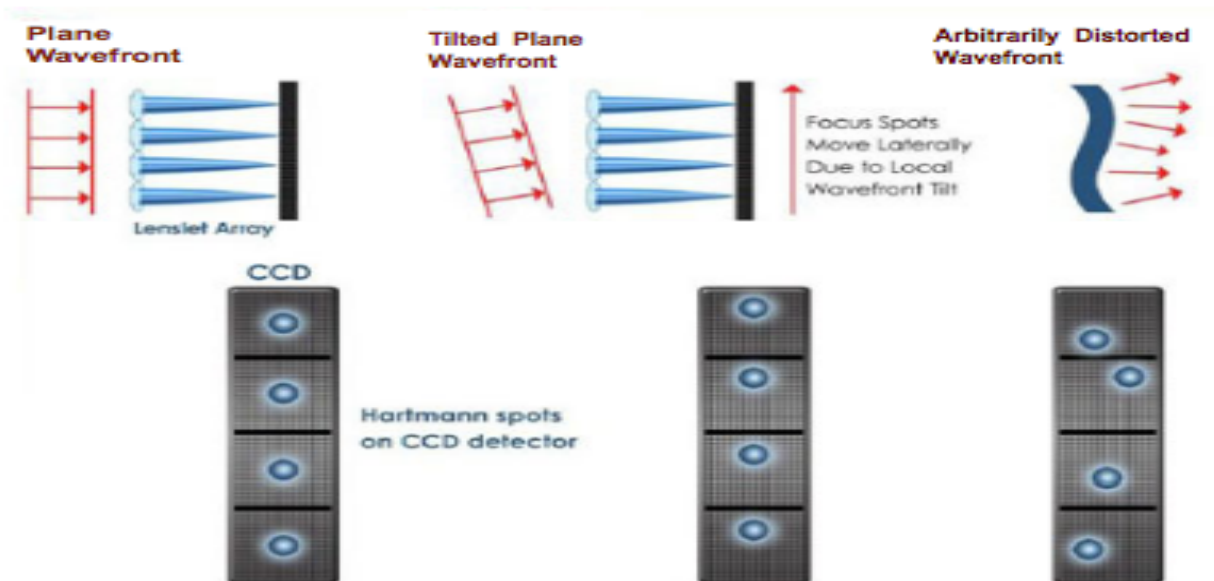


Figure 1: Shack-Hartmann wavefront sensor schematic demonstrating how a perturbed wavefront displaces spot positions. Tilted wavefronts shift the spots in the direction of the tilt.

disturbances to the collimated light beam cause a shift in the spot locations. By analyzing these shifts one can study the origin of the original wavefront disturbance.

Unfortunately, Hartmann's design was limited by two critical factors. First, the aperture he used allowed only a small fraction of light to be transmitted, making it difficult for him to discern the phase shifted wave from the low intensity reference light. Second, the spots created by his aperture suffered from diffraction effects that made it impossible to precisely determine the location of the spot positions (Migdal et al. 230). These limiting factors were compounded by the fact that he lacked the computational power to efficiently handle dynamic experiments. Today, however, researchers have access to more advanced optics and detector technology, giving them the means to overcome these obstacles; Figure 2 shows a functional block diagram of the necessary components of a modern wavefront sensor. Accordingly, modern wavefront sensors are robust and accurate, making them critical components of experiments characterizing the electron density of high density plasmas, powerful instruments for mapping eye lenses and mitigating complex refractive errors, and valuable tools for removing atmospheric distortions from telescopic images (Baker et al. 76).

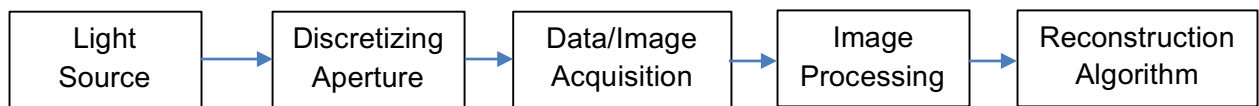


Figure 2: A functional block-diagram of the wavefront sensing device. The first three stages describe the mechanical implementation required to obtain meaningful data. In this project, they were accomplished using a HeNe laser, a microlens array, and a CCD array respectively. The last two blocks are software based, accomplished using National Instruments™ data acquisition software that facilitated computational analysis in Matlab.

Chapter 2: Project Description and Requirements

2.1 Implementation

The mechanical implementation of our wavefront sensor consists of a 635 nm HeNe laser, a beam collimator consisting of a diverging lens of focal length -25 mm followed by a converging lens of focal length 500 mm, two mirrors to redirect the laser beam, a microlens array, and a 480 x 640 pixel CCD array used to image the required spot array. The output of the CCD is read out using National Instruments™ Data Measurement and Acquisition software by means of a PCI 1405 board. The captured CCD image data are then processed and analyzed using Matlab.

Below, we describe in greater detail the important elements of this setup.

2.1.1 Microlens Array

Our microlens array (Appendix C) consists of 4356 converging, fused-silica lenslets photolithographically patterned on a 10 mm x 10 mm square grid (Figure 3). Individual lenslets are separated by 150 microns center-to-center. Each lenslet has a converging focal length of 6.7 mm and transmits light from the deep UV to IR as shown in Figure 4. The noticeable absorption dip near 2700 nm is caused by hydrogen-bonded hydroxyl groups in the fused silica.

The microlens array is perhaps the most essential component of our wavefront sensing system because it discretizes the incoming light to produce a geometrical pattern of spots at the detector plane (CCD camera). The array plays the role of the multi-hole aperture in the original Hartmann sensor but the microlens

implementation is superior because it offers better transmittance and is a clear medium with low index of refraction. Further, it does not suffer from interference effects the way Hartmann's hole-based apertures do.

Lastly, the gaps between elements of our microlens array are coated with chrome to prohibit

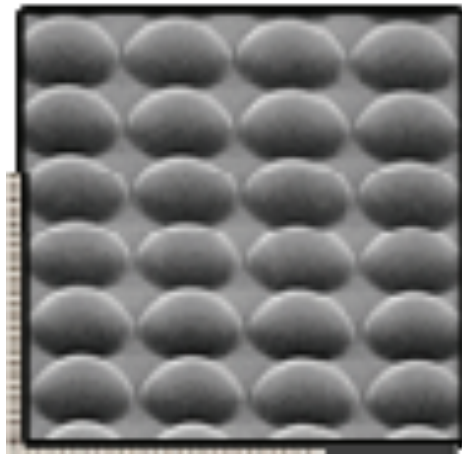


Figure 3: Magnified image of the 10 mm x 10 mm MLA150-7AR microlens array used in this work. The plano-convex, fused-silica lenslets are spaced on a 150 micron pitch. The lens array provides high transmissivity from the deep UV to IR

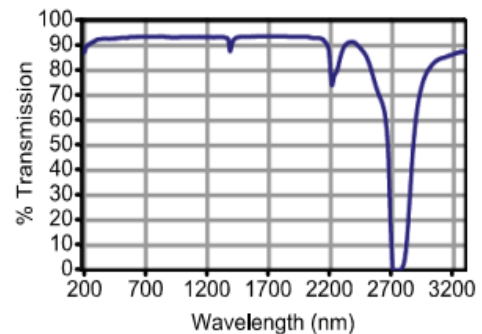


Figure 4: Micro lens array transmission spectrum showing ~ 95% transmission at 635 nm, optimal for the HeNe laser used in our work. The pronounced dip at 2700 nm is due to hydrogen-bonded hydroxyl-groups.

incident source light from passing through the inactive portions of the array. The net result is that our array provides excellent contrast between the focused spots (“signal”) and any scattered light that still exists into the system.

2.1.2 CCD Array

In our design, a 480 x 640 pixel CCD camera was positioned at the focal plane of the microlens array to track the positions of spots created by the lenslets. The CCD camera was biased at +12 V and pixel count data was read out using a National Instruments™ PCI 1405 8-bit data acquisition board. The signal intensity at each pixel was recorded as a number between 0-254 where 254 corresponded to the brightest spot (just below saturation). Though the CCD array was not the ideal size to capture every spot from the microlens array, we were able to capture a 32 x 32 grid of points, providing enough data to reconstruct a significant portion of the wavefront.

There were two minor considerations we needed to account for when using our CCD array to determine spot locations. First, in general, pixel read out is not simultaneous across all pixels of a CCD camera; this means that our uncorrected CCD images suffered from readout lag across points and thus did not completely reflect the state of the system at one instant in time. The second consideration is that there is always noise in a system; in our case this resulted in counts on pixels where ideally none would occur. Both problems were readily addressed by assuming a Gaussian light profile and statistically determining the expected signal intensity arriving at each pixel. Not only did this provide a more precise estimate of the spot location, it also provided a means of estimating the noise floor – enabling background subtraction to be done on each data set (provided the noise was not too large a fraction of the signal intensity). As we experimented with the array, we were able to determine that background noise in the system had a peak magnitude of 20% of the maximum pixel signal. This threshold was necessary to determine so that our algorithm would eliminate any signals below this threshold to prevent them from interfering with later stages of the analysis chain and minimize the loss of real information.

It is important to note that the relatively small size of the CCD camera (480 x 640) used in our work limited the number of lenslet spots that could be imaged in a single experimental run. Moreover, because we were using materials that were readily available, we did not ideally match the non-square geometry of our CCD camera to our square lenslet array. Therefore, as described in more detail below, we compensated for this limitation by systematically analyzing our data

using only a 480 x 480 region of the camera. This greatly simplified the least-squares method analysis programs we developed to perform wavefront reconstruction.

Chapter 3: Wavefront Phase Shift Reconstruction Algorithm

Although the mechanical setup was an important aspect of our wavefront reconstruction device, the computational software development composed a significantly larger portion of the design process because it demanded a deeper understanding of the physics at work in our experiments.

Many algorithms have been developed over the years to enable precise reconstruction of wavefronts. One of the most common approaches to wavefront reconstruction is to use Zernike polynomials to map wavefront curvature. The other is to perform a least-squares fit to the time evolution of bright spot

centroids within the array. This yields the phase introduced by the wavefront disturbance at each point. Our sensor relies on the least-squares method because it provides sufficient accuracy for the purposes of our applications and can be implemented efficiently using MatlabTM. In the following sections, we summarize the different components of our wavefront reconstruction algorithm, focusing on the numerical tactics they exploit and the physics they describe.

3.1 Image Acquisition and Noise Elimination

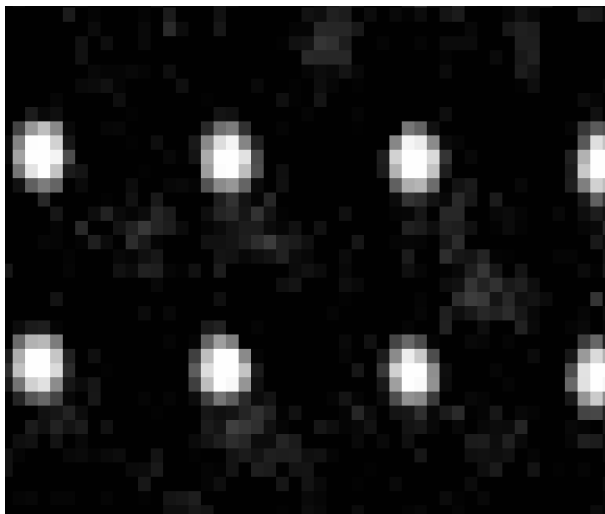


Figure 6: A magnified image of figure 5. Image noise creates ghost spots identifiable here by their non-grid pattern locations and relatively low grayscale intensity compared to the regularly spaced and bright “signal” spots. The brightest spots are 16 pixels apart (center-to-center) and approximately 5-6 pixels in diameter.

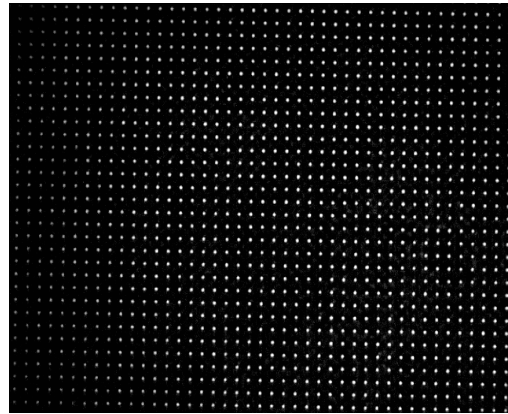


Figure 5: Raw 480x640 pixel image of our micro-lens array as captured by our CCD camera when no wavefront disturbance was present.

We imported CCD images of an unperturbed wavefront into MatlabTM as grayscale .png files after taking snapshots using National InstrumentsTM data acquisition software. This allowed us to study the intensity profile of a “known” incident wavefront and evaluate sources of noise in the system. We found it was easiest to interpret the data (and accurately separate signal from noise) when we converted the grayscale images to a black and white profile, and set a threshold signal intensity at 20% of the

maximum intensity observed. Taking this approach allowed us to filter out most of the noise spots and facilitated the use of a weighted-centroid calculation to do image reconstruction and physics analysis of the real light spots under study.

3.2 Weighted Centroid Determination of CCD Pixel Bright-Spots

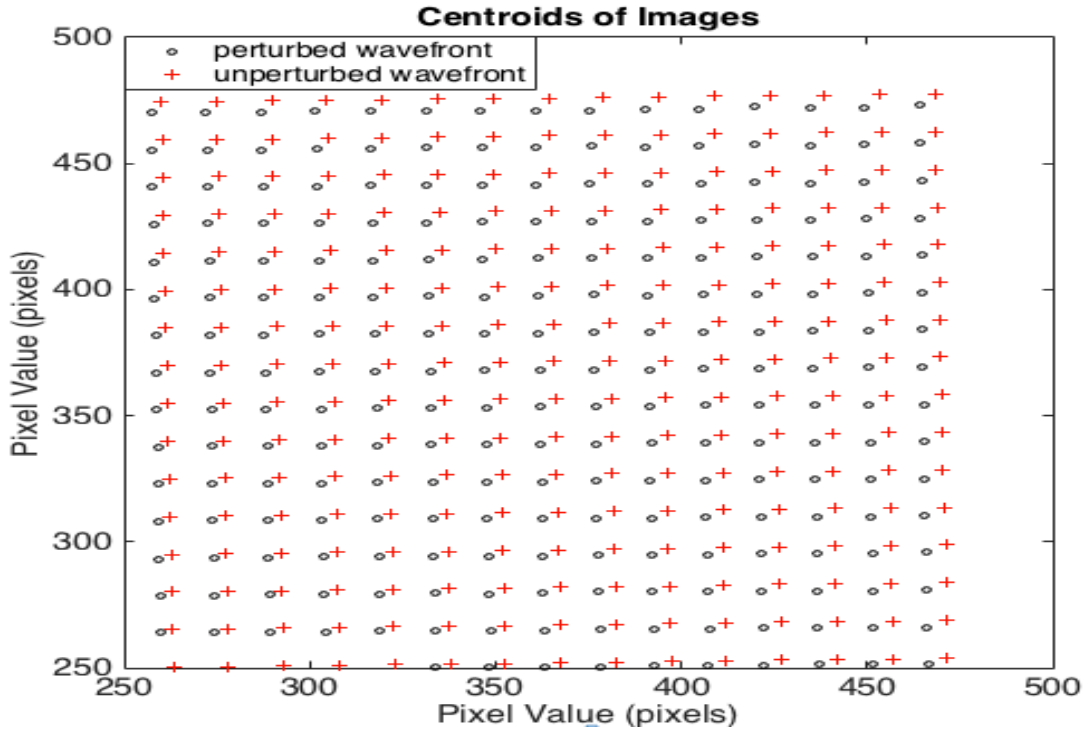


Figure 7: Shifted centroids of signals produced by a thermally perturbed wavefront (perturbation introduced using a hot soldering iron) alongside signal centroids for a flat (unperturbed) wavefront. Centroid locations are shown in terms of their CCD pixel image locations.

We first used our CCD output signal to establish a statistical norm for the pixel positions of the spots resulting from a flat wavefront. To accomplish this task, we first sampled six images, trimmed them to a 480 x 480 pixel area to capture a square pattern of spots that would facilitate further computation, and subjected each image to a discrete-sum, weighted centroid calculation in 2D. The coordinates (x_c, y_c) of each bright-spot centroid in terms of peak energy density were defined using

$$x_c = \sum_{m=1}^{m'} \sum_{n=1}^{n'} I_{m,n} * x_{m,n}$$

$$y_c = \sum_{m=1}^{m'} \sum_{n=1}^{n'} I_{m,n} * y_{m,n}$$

where n' is the number of above-threshold pixels within a particular bright spot labeled m , and I is a decimal value between 0 (least intense) and 1 (most intense). Note that this computation takes into account the intensity of each image pixel. Had we performed a centroid calculation based only on the number of above-threshold pixels for each spot, rather than weighting the results by the measured intensity at each pixel, the dim tails of the gaussian beam through each lenslet could shift the position centroids away from the more meaningful energy centroids.

By thus determining the centroid of each bright spot in the trimmed 32 x 32 spot image, we defined a coordinate system (in units of pixels) to map the location of each light spot on the focal plane. Once this was achieved for each of the 1024 spots, the results from all six test images were signal averaged to improve the centroid resolution. This allowed us to confidently determine the position of each spot and use those positions as a basis for comparison against future images. Once this was achieved, we captured an image for a perturbed wavefront and used the same algorithm to determine bright-spot centroid locations. The results can be seen in the Figure 7, which compares centroid locations from a flat wavefront and one disturbed by a soldering iron.

3.3 Gradient Computation

The statistically determined centroids for the control image (no wavefront disturbance) and those of the distorted image (signal) were then used with the algorithm shown in Appendix C to compute the discretized gradient of each centroid, dz/dx and dz/dy . This was done by measuring the observed directional shifts, Δx and Δy , of high intensity spots in the distorted image relative to the control image and dividing those shifts by the focal length of the microlens array:

$$\frac{dz}{dx} = -\frac{\Delta x}{f}$$

$$\frac{dz}{dy} = -\frac{\Delta y}{f}$$

For these calculations we converted the units of Δx and Δy from pixels to microns (8 microns per pixel).

The algorithm then performed a reverse gradient at each point on the grid. This task was rather difficult to realize because the wavefront had been discretized into points, and a direct integration approach could lead to ambiguous results due to irreducible noise in the experimental system. To circumvent this problem, we utilized Hudgin geometry to determine a least-squares

solution, treating the centroid locations as a square network of nodes related to each other through directional gradients dz/dx and dz/dy . This allowed us to define a system of equations we could then use to find a least-squares solution for the phase shift introduced to a detected signal by external perturbations to the original source wavefront.

3.4 Hudgin Geometry

Figure 8 shows the geometrical convention used to compute the phase of the reconstructed wavefronts using the bright spot locations and the Hudgin technique. Each circle corresponds to a bright spot of our image (signal). The circles are numbered left-to-right, starting from the bottom left corner as shown.

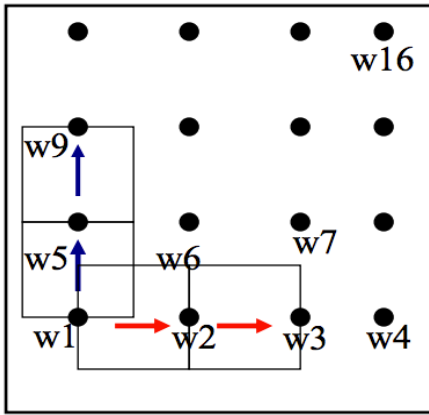


Figure 8: Numbering convention for Hudgin geometry in the case of a 4 x 4 grid of centroids. Numbers increase going left-to-right and down-to-up within the network.

```

[[ 1. -1.  0.  0.  0.  0.  0.  0.  0.  0.  0.  0.  0.  0.  0.  0.]
 [ 0.  1. -1.  0.  0.  0.  0.  0.  0.  0.  0.  0.  0.  0.  0.  0.]
 [ 0.  0.  1. -1.  0.  0.  0.  0.  0.  0.  0.  0.  0.  0.  0.  0.]
 [ 0.  0.  0.  0.  1. -1.  0.  0.  0.  0.  0.  0.  0.  0.  0.  0.]
 [ 0.  0.  0.  0.  0.  0.  1. -1.  0.  0.  0.  0.  0.  0.  0.  0.]
 [ 0.  0.  0.  0.  0.  0.  0.  0.  1. -1.  0.  0.  0.  0.  0.  0.]
 [ 0.  0.  0.  0.  0.  0.  0.  0.  0.  0.  1. -1.  0.  0.  0.  0.]
 [ 0.  0.  0.  0.  0.  0.  0.  0.  0.  0.  0.  0.  1. -1.  0.  0.]
 [ 0.  0.  0.  0.  0.  0.  0.  0.  0.  0.  0.  0.  0.  0.  1. -1.]
 [-1.  0.  0.  0.  1.  0.  0.  0.  0.  0.  0.  0.  0.  0.  0.  0.]
 [ 0. -1.  0.  0.  0.  1.  0.  0.  0.  0.  0.  0.  0.  0.  0.  0.]
 [ 0.  0. -1.  0.  0.  0.  1.  0.  0.  0.  0.  0.  0.  0.  0.  0.]
 [ 0.  0.  0. -1.  0.  0.  0.  1.  0.  0.  0.  0.  0.  0.  0.  0.]
 [ 0.  0.  0.  0. -1.  0.  0.  0.  1.  0.  0.  0.  0.  0.  0.  0.]
 [ 0.  0.  0.  0.  0.  0. -1.  0.  0.  1.  0.  0.  0.  0.  0.  0.]
 [ 0.  0.  0.  0.  0.  0.  0.  0. -1.  0.  1.  0.  0.  0.  0.  0.]
 [ 0.  0.  0.  0.  0.  0.  0.  0.  0. -1.  0.  0.  1.  0.  0.  0.]
 [ 0.  0.  0.  0.  0.  0.  0.  0.  0.  0. -1.  0.  0.  1.  0.  0.]
 [ 0.  0.  0.  0.  0.  0.  0.  0.  0.  0.  0. -1.  0.  0.  1.  0.]
 [ 0.  0.  0.  0.  0.  0.  0.  0.  0.  0.  0.  0. -1.  0.  0.  1.]

```

Figure 9: A matrix that defines relationships between nodes in a Hudgin network for a 4 x 4 geometry. The top half of the matrix represents the nodal relationships of the x-directional gradients and the bottom half represents those in the y-direction. The directional gradients are used in a system of equations to determine a least-squares solution for perturbed wavefront reconstruction.

After determining the statistical energy centroids of all image bright spots as described above, the next step is to define the energy gradient relationships at each node in a matrix; first in the x- and then in the y-direction. This yields a matrix of size $2n(n - 1) \times n^2$, where n is the number of centroids in the grid. This matrix, which we call A , can be seen in Figure 9 and is used to satisfy the relationship:

$$A * \varnothing = g$$

where g and \varnothing are vectors containing the values of the corresponding directional gradients and phase, respectively, for each Hudgin node. The phase information that is embedded in the vector \varnothing can be extracted by inverting matrix A and solving the system:

$$\phi = A^{-1} * g$$

using the Moore-Penrose pseudo-inverse method, a numerical technique that compensates for non-square matrices. Once the inverse is taken and multiplied into the gradient vector g describing the shifted centroid positions, one effectively determines a least-squares solution of the phase at each point in the image, leading to reconstructed waveform data such as those shown in figures 10-18.

Chapter 4: Results

4.1 Flat Wavefront

To test the validity of our algorithm and the overall performance of the measurement system, a sample image was compared against itself to ensure that the result gave a flat phase plot. The results agreed extremely well with expectations, as shown in Figure 10.

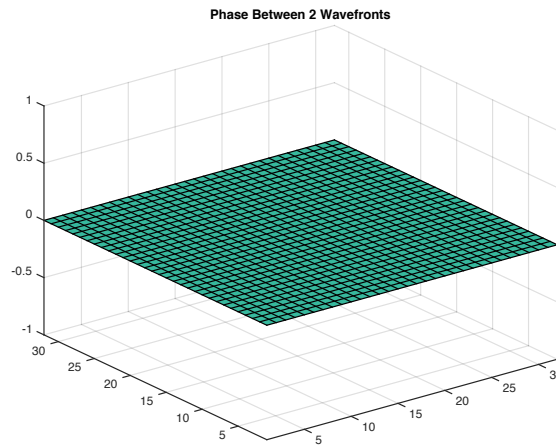


Figure 10: Result of our algorithm and analysis test. A 32-pixel image was independently processed twice, using our SCU software analysis package. The processed data were then compared to each other, pixel-by-pixel, to determine the local phase-shifts between identical test signals. The results were excellent: there was essentially zero detected phase-shift (z-axis) between identical wavefronts imaged across all 1024 pixels (x-y plane) of our test system.

4.2 Experimental Noise

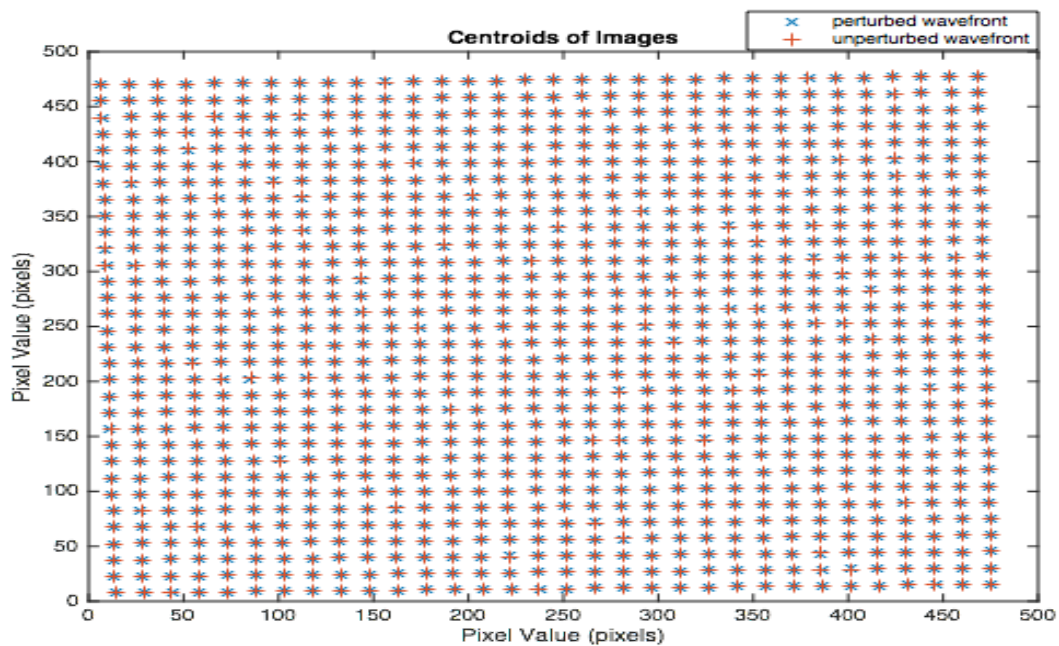


Figure 11: Centroids of a wavefront perturbed by noise and those of a flat wavefront

Our next step was to compare two, flat-wavefront images to determine the noise inherent to the system. Irreducible noise sources included, *e.g.*, CCD detector noise and shot noise, which plays a role in all experimental optics systems. The expectation was that the noise should result in distortion approximately on the order of tens of nanometers, in accordance with similar experiments (Migdal et. al 229). Our computation corroborated this prediction. The resulting reconstructed spot pattern and wavefront phase map are shown in Figures 11 and 12.

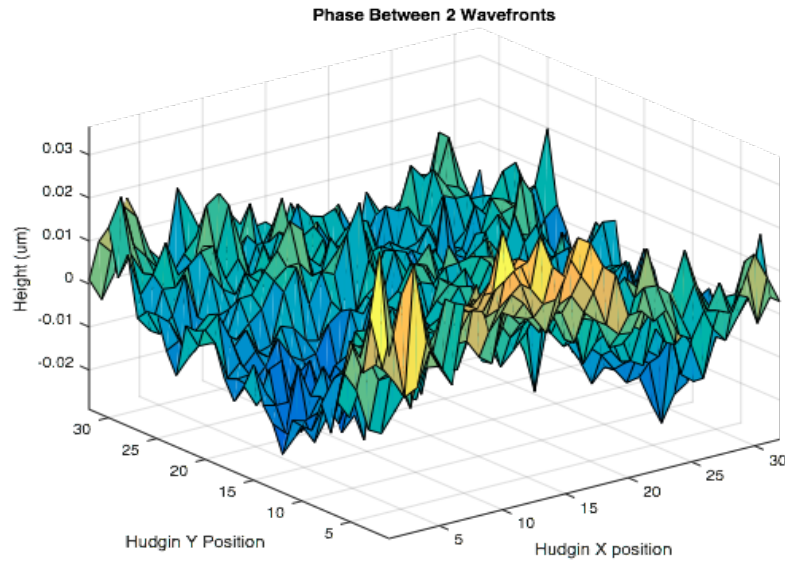


Figure 12: Phase plot showing noise perturbations in our experimental system. These results were determined by comparing two unperturbed wavefront test images.

4.3 Wavefront Perturbed by a Soldering Iron

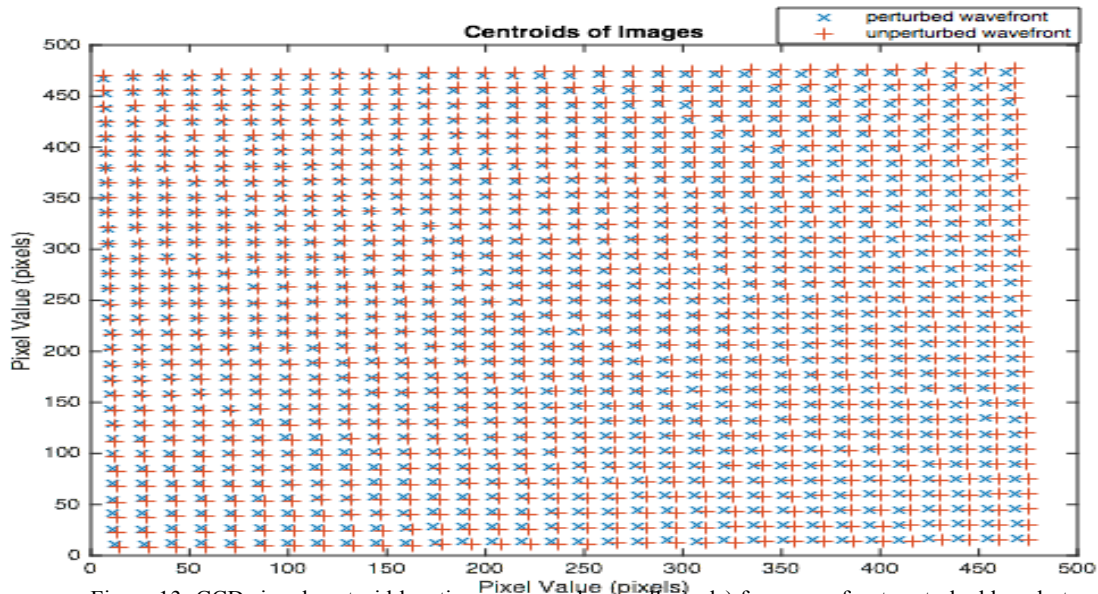


Figure 13: CCD signal centroid locations measured over all pixels) for a wavefront perturbed by a hot soldering iron (x) compared to those for an unperturbed wavefront (+).

We evaluated the performance of our entire system by analyzing CCD images obtained for unperturbed vs. perturbed wavefronts. In these experiments, the wavefront perturbation was created by placing a hot soldering iron beneath the incident beam to generate local turbulent airflow. As shown in Figures 13-14, the results clearly demonstrate curvature in the phase-shift profile consistent with what one might expect given the type of disturbance we introduced. Moreover, the resulting phase shift profile cannot be mistaken for noise because of its distinguishable geometry and the few orders of magnitude increase in signal-to-noise it produced in the observed wavefront phase shifts.

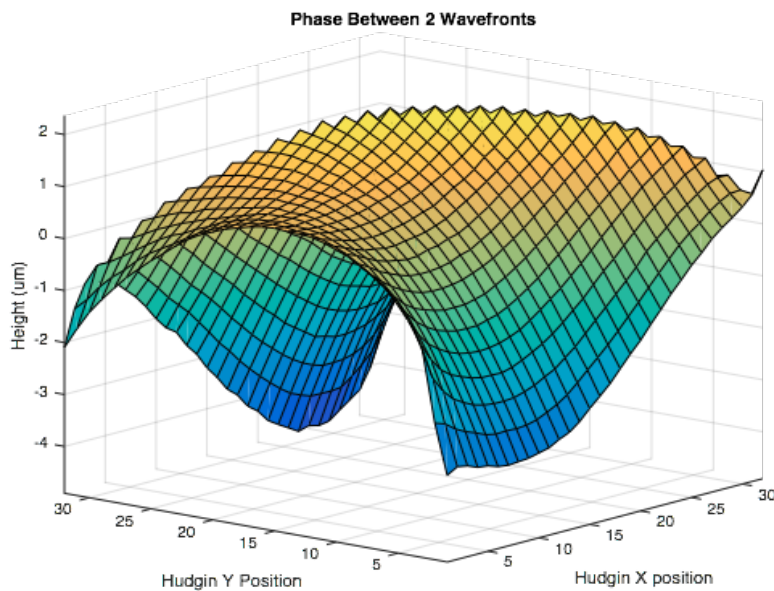


Figure 14: Relative phase disturbance for a wavefront perturbed by a hot soldering iron.

4.4 Diverging Wavefront Perturbed by Mechanical Shear on System

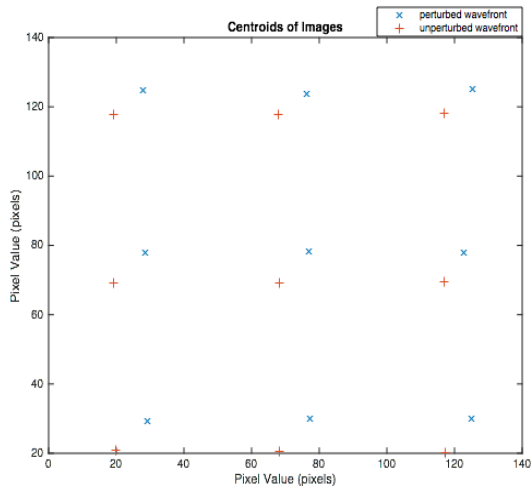


Figure 15: Bright spot centroids for a wavefront subjected to a horizontal shear.

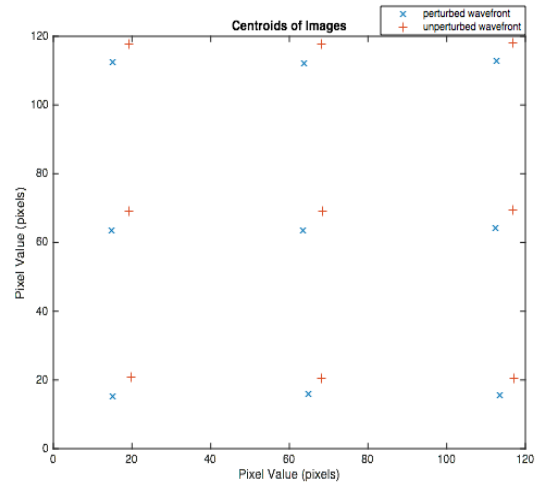


Figure 16: Bright spot centroids for a wavefront subjected to a vertical shear

In a final test, a diverging lens was placed in the signal path to reduce the number of spots projected onto the detector. This resulted in a 3 x 3 grid of centroids in the image plane. The nine spots were then displaced in both the horizontal and vertical directions by rotating the lens holder about its two in-plane axes. The results, shown in Figures 15 -18, yielded the expected results for measurements corresponding to a shear applied in the horizontal direction and the other in the vertical direction.

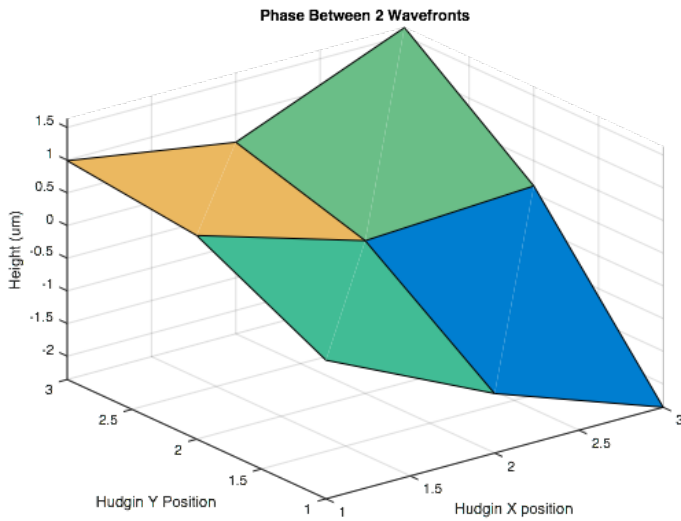


Figure 17: Phase plot resulting from a horizontal shear introduced into the benchtop setup.

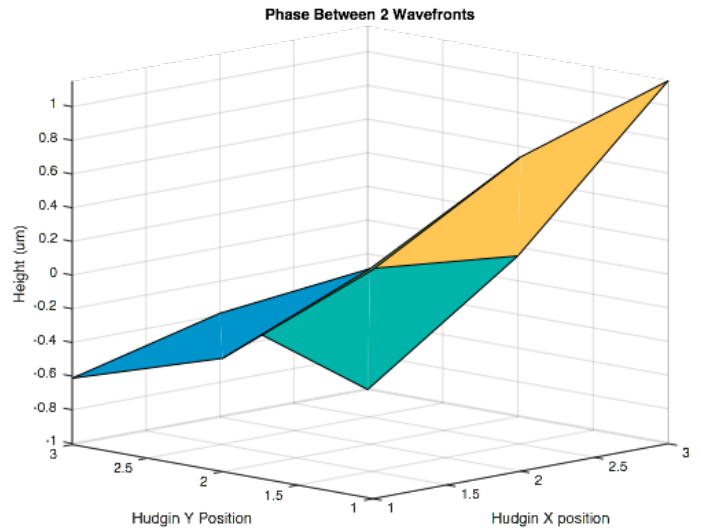


Figure 18: Phase plot resulting from a vertical shear introduced into the benchtop setup.

Chapter 5: Bill of Materials

My design has four critical stages and requires a total of five components for proper function. Fortunately, all of the required components other than two specialized Matlab toolboxes were already available to me through the Physics Department.

However, should the

Components	Thorlabs Wavefront Sensor	Proposed Wavefront Sensor
Laser	\$1000	\$1000
Collimating Lenses	N/A	\$100
Microlens Array	N/A	\$400
CCD Array	N/A	\$65
Matlab Toolboxes	N/A	\$100
Purchase Price	\$4000	N/A
TOTAL COST	\$5000	\$1665

department wish to construct an additional wavefront sensor, the total cost would be \$1665 (+ tax), as summarized in the accompanying table. Considering that all of the necessary components have over a decade-long lifespan, no additional funds would be required for long-term use of our wavefront sensor in SCU labs.

Commercial wavefront sensors are three times more expensive than our design, and offer far less utility in a teaching lab because they are prepackaged and designed to provide plug-and-play operation. In contrast, our wavefront sensor requires the user to assemble and align the device before use, thus offering students additional laboratory experience and the important opportunity to learn through trial and error. Our device can also facilitate research in a variety of specialized areas within optics, thus opening the door for additional funding opportunities for the Department of Physics. Accordingly, the return on investment (even beyond important educational rewards), will be a function of how many new and related research proposals get funded.

Chapter 6: Professional Issues and Constraints

6.1 Ethical Analysis

I maintain that this wavefront sensor has very few, if any, ethical dilemmas associated with its development. Nevertheless, it is my aim to convince the reader that this statement is true in all regards: organizationally, socially, and in terms of product development and deployment. Below, I will examine each of these criteria separately, and verify that my team is acting and will act ethically. I will confirm, that our new device and measurement system has zero associated negative impacts on society,,that our group takes its duty to potential users seriously. and that we maintained the highest standards of integrity in all related research and design processes carried out in the completion of this project.

6.1.1 Organizational Considerations

Considering the team consists of only myself and my advisors, the duty of upholding ethical standards within my team falls largely on my shoulders. As such, I have made sure to analyze the constructive and destructive effects related to my design. Having researched the potential consequences, I maintain that the project is ethical in large part because it is based on inherently safe technology and one would be hard pressed to apply it in a destructive context. Verifying that my full team is acting ethically in a global context is perhaps best evaluated by considering the ethical reputation of my advisors, all of whom are active and productive researchers with strong professional reputations and clear commitments to always doing R&D in a fair and ethical and responsible manner.

6.1.2 Social Considerations

As a designer, my ethical duty towards potential users is to supply them with accurate and complete information about the uses and limitations of my product. More specifically, I must be sure to inform users of the compatibility of my wavefront sensor with other optical systems, standard laboratory products, and common computational software used in many labs throughout the world. In doing so, I hold myself to the highest degree of marketing integrity so that consumers are not mislead into purchasing my product if it does not integrate well with their systems. This effectively eliminates the possibility of litigation against my team as a result of fraudulent marketing practices. Future social responsibility of using the sensor will be transferred to the consumer. I maintain that this assertion is fair and ethical because the user will have all

the information necessary to make an informed decision about whether or not to use my product, and how to use it safely.

6.1.3 Research & Design Considerations

The most noticeable ethical implications for this project relate to the research and design phase, and how I report the results of that work. I have maintained the highest standards of research integrity by avoiding plagiarism, using appropriate citations of others' work, and giving credit to those who supported the R&D project from beginning to end. On top of my own personal sense of integrity, I allege that I have established the checks and balances necessary to consistently achieve this level of honesty while working with my advisors, potential consumers, and others in academia at-large.

The first system in place to curb any attempt of taking credit for the written work of others is turnitin.com. This website can be used to check if work submitted by one author has in fact been written by another. In my case, my advisors checked often on my progress and quality of data. They emphasized the need to take multiple data sets to ensure the robustness of the system and the repeatability of experiments using my device. I learned from my advisors how to scrutinize results and how to work carefully to avoid the possibility of having false positive results occur because of a hidden design error.

I have the ability to corroborate science results obtained with my wavefront sensor by comparing them to data published by others working on similar experiments but with different sensor designs. Clearly the fundamental science results of experiments should agree, independent of the exact type of sensor used to make the measurements.

Separately, I am fortunate that my design is being used for academic purposes and not in a business context because it leaves me free to disclose all aspects of my experimental methods and results; I do not fear competition because I only want to advance the education of students without concern for profits. In fact, the physics department specifically asked me to produce a detailed report of my design specifications, process, and results so optics students can use my system optimally in the future. Thus, I am ethically obligated to write my report for future physics students clearly and openly so they can use my results as a foundation for any future improvements to the wavefront sensor system designed and built for this senior thesis.

6.2 Health and Safety

There is only one aspect of the design with the potential to harm someone using our sensor. The unlikely but potential source of danger stems from the use of a HeNe laser to produce our wavefront sensor input signals. In the standard mode of operation, a HeNe laser emits non-ionizing radiation at 635 nm, and is considered minimally dangerous when used as expected. However, an inherent risk associated with using any laser is the risk that laser light can shine in the eyes of a user or bystander, potentially causing blindness. Fortunately, there is an easy way to mitigate this potential problem – users and anyone else exposed to the system must simply wear appropriate laser laboratory glasses for protection. There are no other health and safety concerns associated with the use of this device.

6.3 STS and Civic Engagement

I contend this project clearly demonstrates social sustainability in its commitment to advancing the laboratory experience of undergraduate physics majors and others who take Physics 113 or do optics research at SCU. The main objective of this project was to provide a means by which students can analyze phenomena invisible to the naked eye. Our new wavefront sensor will help students achieve a deeper understanding of advanced electromagnetic concepts taught in class, and provide them tangible data that can corroborate theoretical claims. Moreover, this technology can be used by students who wish to conduct further research in the field. Successful work in this area will positively impact academia as a whole, and perhaps also industry. Thus, I contend it is clear that our wavefront sensor is socially responsible and sustainable and offers many positive short-term and potential long-term benefits.

6.4 Manufacturability & Usability

The user interface coupled to this device is quite simple for undergraduate physics students to operate. While they may have to reposition or realign some of the sensor components before use (depending on when certain components were last used and for what), doing so will enhance their laboratory experience by helping them become more familiar with common elements of an optics lab. As for the sensor software we developed, the user will have to do very little to operate the wavefront reconstruction algorithm. There are only two lines of code student users will need to edit – these are the names of the two images (reference signal and perturbed signal) they will be using for analysis. However, the entire code is filled with comments to help users follow the logic and to make it easy for users to potentially improve the code in the future.

6.5 Sustainability and Environmental Impact

Unlike other engineering projects, my design is predominantly software based; accordingly, there are very few components associated with the design that have the potential to harm the environment. More specifically, a majority of the physical components are lenses and mirrors made of glass, a very environmentally friendly material because it can be recycled repeatedly. That leaves only two items of concern in regards to this project: the HeNe laser and the CCD array which will be problematic only at the end of their approximately ten year product lifespan. Fortunately, both the CCD array and the HeNe laser can be sent back to the manufacturer for proper disposal and recycling. Thus, I believe it is apparent that my design satisfies the criteria of being environmentally sustainable.

In addition, there is little need to be concerned about being able to operate our wavefront sensor for many years. The components in this project all have lifetimes that span almost a decade. The only foreseeable concern for the project in the long run stems from the possibility that the equipment be damaged by accident during its use. Fortunately, each component of our system can be replaced by substitute products that are equally functional and applicable to this design.

Lastly, this project requires significantly less power than most household items (the laser and CCD array operate at 0.8-2W and 1.8W respectively). Accordingly, there is a minimal energy demand associated with the wavefront sensor. In short, I believe it is clear that the wavefront sensor demonstrates its sustainable nature with respect to materials used, its energy resources, and longevity.

Chapter 7: Conclusion


Given the excellent agreement between our experiment results and theoretical predictions, it is clear that our full wavefront sensor package is functional and accurate. It could handle disturbances resulting in micron length perturbations to the wavefront and the system offered precision to the diffraction limit of our optic, of order tens of nanometers. Additionally, we proved the algorithm is robust and capable of facilitating and enhancing a range of laboratory experiments. And finally, we clearly demonstrated that this project has few ethical, safety, or sustainability concerns, making this project worth implementing in the Santa Clara Physics Department.

Works Cited

- Baker, K. L. "Least-squares Wave-front Reconstruction of Shack-Hartmann Sensors and Shearing Interferometers Using Multigrid Techniques." *Rev. Sci. Instrum. Review of Scientific Instruments* (2005): 76-78. Print.
- Baker, K. L., J. Brase, M. Kartz, S. S. Olivier, B. Sawvel, and J. Tucker. "The Use of a Shack–Hartmann Wavefront Sensor for Electron Density Characterization of High Density Plasmas." *Rev. Sci. Instrum. Review of Scientific Instruments* (2002): 73-77. Print.
- Li, Chenhui, Gunnsteinn Hall, Xuefeng Zeng, Difeng Zhu, Kevin Eliceiri, and Hongrui Jiang. "Three-dimensional Surface Profiling and Optical Characterization of Liquid Microlens Using a Shack–Hartmann WaveFront Sensor." *Appl. Phys. Lett. Applied Physics Letters* (2011): 98-101. Print.
- Migdał, Piotr, Piotr Fita, Czesław Radzewicz, and Łukasz Mazurek. "Wavefront Sensor with Fresnel Zone Plates for Use in an Undergraduate Laboratory." *Am. J. Phys. American Journal of Physics*(2008): 229-235. Print.
- Richter, H., M. Greiner-Bär, N. Deßmann, J. Pfund, M. Wienold, L. Schrottke, R. Hey, H. T. Grahn, and H.-W. Hübers. "Terahertz Wavefront Measurement with a Hartmann Sensor." *Appl. Phys. Lett. Applied Physics Letters* (2012): 101-104. Print.

Appendices

Appendix A:



Self-Contained HeNe Laser: 0.8 mW, Polarized, 120 VAC

HNL5008L 

Description

Thorlabs' cylindrical, low-power, red (632.8 nm) Helium-Neon lasers are available with output powers from 0.8 to 2.0 mW. Thorlabs offers these 632.8 nm lasers with either linear (>500:1) or random polarization and beam divergences ranging from 1.3 to 1.7 mrad.

Specifications

General	
Wavelength	632.8 nm
Minimum Output Power (TEM ₀₀)	0.8 mW
Minimum Polarization Ratio	500:1
Beam Diameter (TEM ₀₀ , 1/e ² points + 3%)	0.48 mm
Beam Divergence (TEM ₀₀ , +3%)	1.7 mrad
Mode Purity (TEM ₀₀)	>95%
Longitudinal Mode Spacing	1090 MHz
Maximum Noise (RMS) (30 Hz to 10 MHz)	1.0%
Maximum Drift*	± 2.5%
Maximum Mode Sweeping Contribution	10%
Operating Voltage (± 100 V)	1250
Operating Current (± 0.1 mA)	4 mA
Maximum Starting Voltage	10 kV DC

*With respect to mean power over 8 hours.

Physical / Mechanical	
Maximum Warm-Up Time (95% Power)	10 min
Storage Lifetime	Indefinite (Hard-Sealed)
Static Alignment	Approximately 1.75" from Base
Laser Weight	1.1 lbs (0.5 kg)

Environmental	
Operating Temperature	-40 to 60 °C
Non-Operating Temperature	-40 to 100 °C
Operating Altitude	0 to 10,000 ft
Non-Operating Altitude	0 to 70,000 ft
Relative Humidity (Non-condensing)	Non-Condensing
Shock	25 g for 11 ms
	100 g for 1 ms

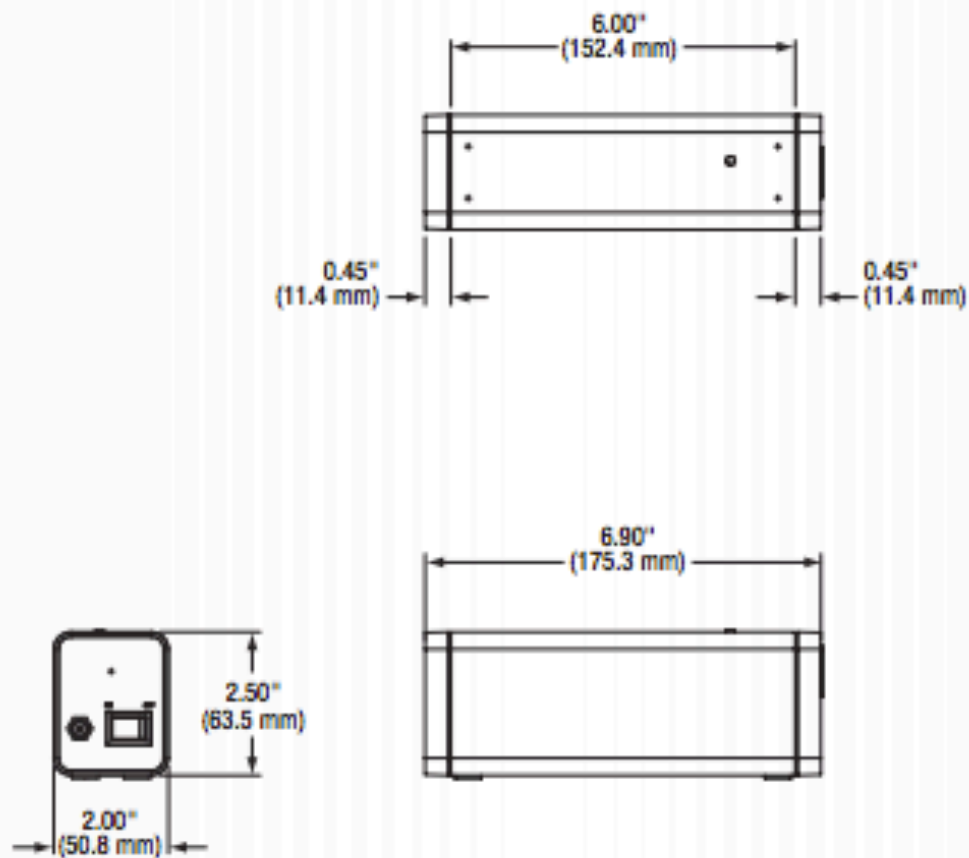
Safety	
CDRH/IEC 60825-1 Class	IIa/3R



Specifications subject to change without notice

November 10, 2011
22152-S01, Rev A

Drawings



Low-Cost Single-Channel Color or Monochrome Image Acquisition

NI PCI-1405

- Color or monochrome image acquisition
- 1 NTSC, PAL, RS-170, or CCIR input
- Partial image acquisition with onboard programmable region of interest
- Onboard pixel decimation
- Programmable gain and offset
- 1 external trigger/digital I/O line

Operating Systems

- Windows 2000/NT/XP

Recommended Software

- LabVIEW
- Measurement Studio
- Vision Development Module
- NI Vision Builder for Automated Inspection

Driver Software (included)

- NI-IMAQ

NEW



Overview

For low-cost analog color image acquisition, National Instruments offers the PCI-1405, which acquires analog video input from standard color or monochrome cameras. The NI PCI-1405 comes with easy-to-use image acquisition driver software which can acquire, save and display images. Unlike multimedia "frame grabbers", the PCI-1405 features increased image processing throughput, such as partial image acquisition with programmable region of interest.

Easy-to-Use Driver Software

National Instruments NI-IMAQ driver level software offers the most comprehensive software interface for image acquisition. NI-IMAQ is included with the PCI-1405 board, as well as NI Measurement & Automation Explorer (MAX) for easy configuration of cameras. Using NI-IMAQ, you can quickly and easily acquire, save, and display images without low-level programming. You can program your image acquisition application in LabVIEW, LabWindows/CVI, and Measurement Studio. In addition, NI-IMAQ controls the PCI-1405 digital I/O line.

Performance Gains with Partial Image Acquisition

The PCI-1405 includes features that improve overall image acquisition and image processing speed. You can choose to acquire only a portion of the image using the onboard programmable ROI

(region of interest) feature. You can configure the size of the acquired image using MAX, or use the ROI tools in the NI-IMAQ driver software to transfer only a subset of the image to PC memory for processing. Partial image scanning results in fewer pixels to process. For example, using partial image scanning, you can reduce a 640 by 480 image to a 400 by 400 image and increase your processing speed by operating on 48 percent fewer pixels.

Hardware

PCI Interface

The PCI bus is the electrical interface for the PCI-1405. The National Instruments custom MITE ASIC for interfacing to the PCI bus offers the highest image acquisition performance available. The MITE ASIC can transfer data at a maximum sustained rate of 100 MB/s in master mode to maximize the use of the available PCI bandwidth.

Onboard Memory

The PCI-1405 has 16 MB of onboard memory, useful for temporary storage of images being transferred to the PCI bus.

Trigger and Strobe

You can use the digital I/O line as an input to trigger image acquisition or as an output to control solenoids, solid-state relays, or strobes.



Low-Cost Single-Channel Color or Monochrome Image Acquisition

Programmable Gain and Offset

The PCI-1405 has programmable gain and offset circuitry for optimizing the input signal range.

I/O Connector and Cabling

Two external BNC connectors are used for the video source and digital I/O line. The PCI-1405 is shipped with a 2 m BNC cable.

Color Pattern Matching

Use color pattern matching to locate quickly known reference patterns, or fiducials, in a color image. With color pattern matching, you create a model or template of an object. The search tool first

scans the image to match the color distribution, and then scores the match for shape. The score relates to how closely the model matches the pattern found. You should use color pattern matching to locate reference patterns that the color and spatial information in the pattern fully describe. Color can often simplify a monochrome problem by improving contrast or separation.

Ordering Information

NI PCI-1405778838-01
Includes NI-IMAQ software and 2 m BNC-BNC-1 cable

Specifications

Typical for 25 °C unless otherwise noted.

Available Formats

RS-170, NTSC	25 frames/interlaced
CCIR401, PAL	25 frames/interlaced

Video Input

Gain(s)	1 monochrome or color
Video I/O	Single-ended (BNC)
Input impedance	75 Ω
Bandwidth	Typical: 33 MHz (color)
Input 10-bit range	11.25 MV (monochrome)

A/D Conversion

Conversion	256 digital
SNR	> 47 dB (monochrome)
RMS noise	< 0.5 DN _{rms}
SNR	Typical: 48 dB

External Synchronization and Trigger Signals

Trigger source	75 Ω
Trigger polarity	Programmable (positive or negative)
Minimum detectable pulse width	22 ns

White(s)	2 V
White(s)	0.5 V

Pixel Clock

RS-170, NTSC	15.27 MHz (color)
CCIR, PAL	16.75 MHz (color)
Pixel rate	4/line
Line rate	< 1/line

PCI Interface

Bus interface	Master, slave
Bus master performance	100 MB/s (DMA)

Power Requirement

+5 VDC (V _{CC})	1.25 A
+12 VDC (V _{CC2})	400 mA

Physical

Dimensions	16.7 by 17.5 cm (6.2 by 6.9 in.)
------------	----------------------------------


Environment

Operating temperature	0 to 55 °C
Storage temperature	-20 to 70 °C
Relative humidity	5 to 95%, noncondensing

Appendix C:

Product Specification Sheet

Microlens Arrays



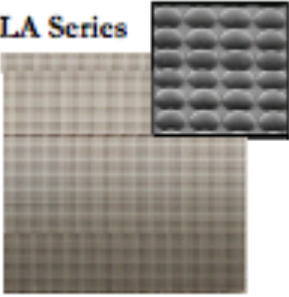
Description

Thorlabs Microlens Arrays are best suited for Shack-Hartmann sensor applications. Both lenslets are made from fused silica for excellent transmission characteristics from the deep UV to IR and have a plano-convex shape that allows nearly refraction limited spots.

The lenses are formed using photolithographic techniques based on semiconductor processing technology, which allows for excellent uniformity in the shape and position of each microlens, unlike some microlens arrays produced from molded epoxy.

The MLA150-5C has a chrome mask that blocks light from being transmitted unless it goes through a microlens and therefore increases image contrast. The MLA150-7AR and MLA300-14AR have a broadband AR coating to reduce surface reflections in the 400-900nm spectral region to below 1%.

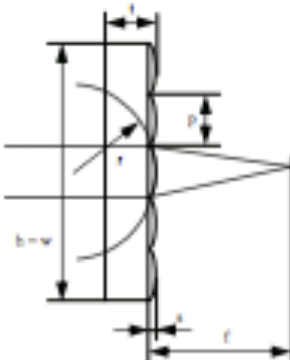
MLA Series



Specifications

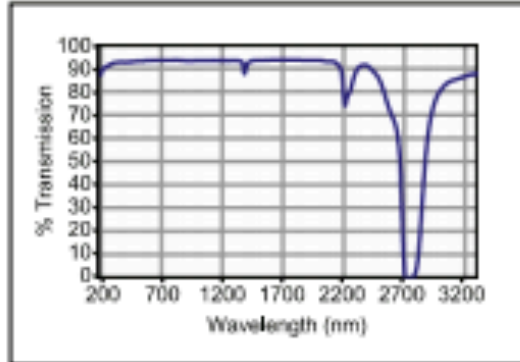
Parameters	MLA150-5C	MLA150-7AR	MLA300-14AR
Substrate Material	Fused Silica (Quartz)		
Wavelength Range	From DUV to IR		
Array Size and Type	10 x 10 mm, Square Grid		
Lens Type	Round, Refractive, Plano-Convex		Square, Refractive, Plano-Convex
Lens Pitch / Diameter	150 μ m / 146 μ m		300 μ m square
Focal Length	5.2 mm	6.7 mm	18.6 mm
AR-Coating	no	Yes, Reflectivity < 1% Within 400 ... 900 nm	
Chrome Apertures	Yes, Around Microlenses	no	
Geometric Parameters			
h, w	10 mm	10 mm	10 mm
t	1.24 mm	1.19 mm	1.20 mm
p	150 μ m	150 μ m	300 μ m
s	1.12 μ m	0.87 μ m	1.31 μ m
r	2.380 mm	3.063 mm	8.6 mm
f	5.2 mm	6.7 mm	18.6 mm

Drawings

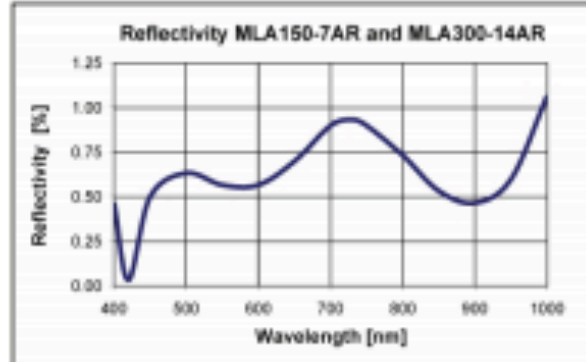


1637- 01/10/10
Specifications subject to change without notice.

Wavelength Characteristics

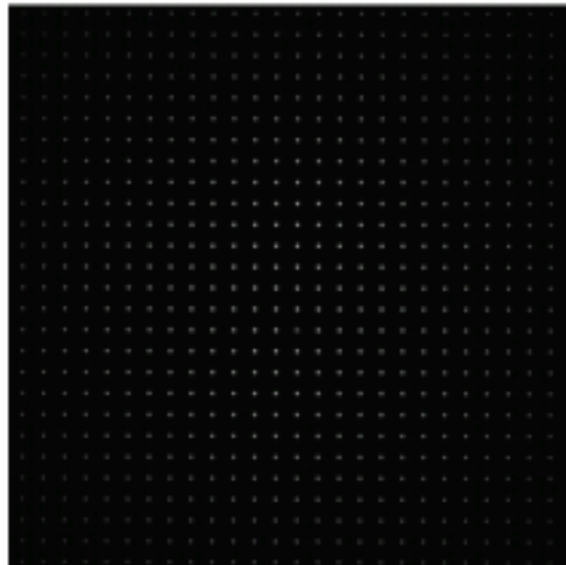


Typ. Transmission of Fused Silica Material



Reflectivity including AR - Coating

Spotfield derived with the MLA150-5C Microlens Array



WEEE

As required by the WEEE (Waste Electrical and Electronic Equipment Directive) of the European Community and the corresponding national laws, Thorlabs offers all end users in the EC the possibility to return "end of life" units without incurring disposal charges.

This offer is valid for Thorlabs electrical and electronic equipment

- sold after August 13th 2005
- marked correspondingly with the crossed out "wheelie bin" logo (see fig. 1)
- sold to a company or institute within the EC
- currently owned by a company or institute within the EC
- still complete, not disassembled and not contaminated

As the WEEE directive applies to self contained operational electrical and electronic products, this "end of life" take back service does not refer to other Thorlabs products, such as

- pure OEM products, that means assemblies to be built into a unit by the user (e. g. OEM laser driver cards)
- components
- mechanics and optics
- left over parts of units disassembled by the user (PCB's, housings etc.).

If you wish to return a Thorlabs unit for waste recovery, please contact Thorlabs or your nearest dealer for further information.

Waste Treatment on Your Own Responsibility

If you do not return an "end of life" unit to Thorlabs, you must hand it to a company specialized in waste recovery. Do not dispose of the unit in a litter bin or at a public waste disposal site.

Ecological Background

It is well known that WEEE pollutes the environment by releasing toxic products during decomposition. The aim of the European RoHS directive is to reduce the content of toxic substances in electronic products in the future.

The intent of the WEEE directive is to enforce the recycling of WEEE. A controlled recycling of end of life products will thereby avoid negative impacts on the environment.



Crossed out "wheelie bin" symbol

USA, Canada, & S. America
Thorlabs Inc.
400 Route 206
Newark, NJ 07102 USA
Tel: +1-973-327-1227
Fax: +1-973-326-5680
www.thorlabs.com
email: feedback@thorlabs.com

Europe
Thorlabs GmbH
Hans-Böckler-Str. 6
65251 Dietrich, Germany
Tel: +49-624111-3996-0
Fax: +49-624111-4994-89
www.thorlabs.com
email: Europe@thorlabs.com

UK and Ireland
Thorlabs LTD
1 Sains Thomas Place, Ely
Cambridge CB7 4EK, GB
Tel: +44-1353-634440
Fax: +44-1353-634444
www.thorlabs.com
email: salesuk@thorlabs.com

Scandinavia
Thorlabs Scandinavia AB
Box 140 90
400 20 Göteborg, Sweden
Tel: +46-31-713-50-00
Fax: +46-31-703-40-45
www.thorlabs.com
email: scandinavia@thorlabs.com

Japan and Asia
Thorlabs Japan Inc.
5-17-1, Chitoseki
Bunkyo-Ku, Tokyo 112-0011, Japan
Tel: +81-3-5979-8899
Fax: +81-3-5979-7395
www.thorlabs.jp
email: sales@thorlabs.jp



16137-02/01/0010

Specifications subject to change without notice.

Appendix D:

```
%% Senior Design MATLAB Phase Calculator Code

% Image Processing

tic;
%The slope of the spots on array (in degrees)
theta = -.94529;

%Read in data from disturbed image
I = imread('c2.png');

%Obtain centroids of disturbed image

[centroids,I,Bw1] = centroidfinderC(I,theta);

%Read in data from reference image
I2 = imread('mla1.png');

%Obtain centroids of reference image
[centroids2,I2,Bw2] = centroidfinder(I2,theta);

% Centroid Sorting

%Pixel Spacing in microns
pix_space = 8;

%Sort centroids from first image and convert to units of microns
centroids = centroidsort(centroids,theta);
x1 = pix_space*centroids(:,1);
y1 = pix_space*centroids(:,2);

%Sort centroids from second image and convert to units of microns
centroids2 = centroidsort(centroids2,theta);
x2 = pix_space*centroids2(:,1);
y2 = pix_space*centroids2(:,2);

% Gradient Determination

delta_x = x2 - x1;
delta_y = y2 - y1;

%This is the focal length of the microlens array in microns
f = 6700;
%Determine the x-directional gradient
grad_x = -delta_x/f;
%Determine the y-directional gradient
grad_y = -delta_y/f;

% Hudgin Geometry
%Dimensions of the square area composed of centroids

dim_s = sqrt(length(x1));
%Dimension used in hudgin geometry
```

```

dim_m = dim_s*(dim_s-1);

%Get hudgin matrix and vector of gradients
[xygrad_m, grad] = hudgin_geom(dim_s,dim_m,grad_x,grad_y);

% Phase Determination

%Take the Pseudo-inverse of non-square matrix
xygrad_inv = pinv(xygrad_m);

%Compute the phase at each point on centroid square
%150 microns is the pitch of the microlens
Phase = 150*xygrad_inv*grad;
%Turn the Phase into a plottable matrix of values
P = vec2mat(Phase,sqrt(length(x1)));
toc

figure(1)
plot(centroids(:,1),centroids(:,2),'ok','markers',4)
hold on
plot(centroids2(:,1),centroids2(:,2),'+r','markers',6)
title('Centroids of Images')
xlabel('Pixel Value (pixels)')
ylabel('Pixel Value (pixels)')
legend('perturbed wavefront','unperturbed wavefront')
set(gca,'fontsize',12)
figure(2)
surf(P)
title('Phase Between 2 Wavefronts')
axis([1, size(P,1), 1, size(P,2), min(min(P)), max(max(P))]);
xlabel('Hudgin X position')
ylabel('Hudgin Y Position')
zlabel('Height (um)')
figure(3)
scatter3(x2,y2,Phase,'*')
xlabel('X position (um)')
ylabel('Y Position (um)')
zlabel('Height (um)')

function [centroids,I,Bw] = centroidfinder(I,theta)

theta = theta;
I = mat2gray(I); %Turn image into grayscale values
I = I - 0.2*max(max(I)); %Subtract out noise
I = I(:,640-475:640); %Trim image to fit a square of centroids

Bw = I > .15; %Set the greyscale threshold

%Obtain list of centroid positions, areas of spots, the pixel coordinates,
%and respective intensity values

stat = regionprops(Bw, I,'WeightedCentroid','Area','PixelList');

count = 1;

```

```

%Filter out noise spots
for x = 1: numel(stat)

    if stat(x).Area > 6 & stat(x).PixelList(:,2) > 5

        centroids(count,:) = [stat(x).WeightedCentroid(1)
stat(x).WeightedCentroid(2)];
        count = count+1;

    end

end

end

function centroids = centroidsort(centroids,theta)

theta = -theta;

temp = centroids(:,1);
[temp,X] = sort(temp, 'ascend');

for n = 1:length(X)

    temp2(n,1) = centroids(X(n),2);

end

temps = [temp temp2];
z = sqrt(length(X));

for n = 0:z-1

    xbin(1:z,n+1) = temps((n*z+1):((n+1)*z),1);
    ybin(1:z,n+1) = temps((n*z+1):((n+1)*z),2);

end

for n = 0:z-1

    [ybin_v,ind] = sort(ybin(:,n+1), 'ascend');
    ind_m(:,n+1) = ind;
    ybin(:,n+1) = ybin_v;

    xbin(1:z,n+1) = xbin(ind(1:z),n+1);

end

xbin = xbin';
ybin = ybin';

centroids(:,1) = reshape(xbin,[],1);
centroids(:,2) = reshape(ybin,[],1);

```

```

end
function [xygrad_out, grad] = hudgin_geom(dim_s,dim_m,grad_x,grad_y)

count = 1;

%Define x directional gradient vector
for n = 1:length(grad_x)

    if mod(n,dim_s) == 0

        count = count;

    else

        grx(count) = grad_x(n);
        count = count + 1;

    end

end

%Define y directional gradient vector
for n = 1:(length(grad_y)-dim_s)

    gry(n) = grad_y(n);

end

%Combine x and y gradients into a single vector
grad = [grx';gry'];

%Initialize matrix for x and y hudgin gradient relationships
xgrad_m = zeros(dim_m,dim_s^2);
ygrad_m = zeros(dim_m,dim_s^2);
xcount = 1;

%Define x-directional hudgin relationships
for n = 1:dim_m

    xgrad_m(n,xcount) = 1;
    xgrad_m(n,xcount+1) = -1;

    if xcount == dim_s-1

        xcount = xcount+2;
        count = 1;

    else

        xcount = xcount+1;
        count = count+1;

    end

end

```



```
end

%Define y-directional gradient relationships
for n = 1:dim_m

    ygrad_m(n,n) = -1;
    ygrad_m(n,n+dim_s) = 1;

end

%Combine x and y-directional gradient relationships into one matrix
xygrad_out = [xgrad_m; ygrad_m];

end
```